

Influence of *in situ* applied ultrasound during Si⁺ implantation in SiO₂ on paramagnetic defect generation

M. Jivanescu,¹ A. Romanyuk,² and A. Stesmans^{1,a)}

¹Department of Physics, University of Leuven, Celestijnenlaan 200 D, B-3001 Leuven, Belgium and Institute for Nanoscale Physics and Chemistry (INPAC), University of Leuven, Celestijnenlaan 200 D, B-3001 Leuven, Belgium

²Institute of Physics, University of Basel, Klingenbergstrasse 82, 4056 Basel, Switzerland

(Received 18 December 2009; accepted 18 February 2010; published online 3 June 2010)

Electron spin resonance (ESR) results are presented on the influence of *in situ* ultrasound treatment (UST) during implantation at 300 K of Si⁺ ions into thermal SiO₂ on (100)Si before and after subsequent high-temperature (T) annealing (1100 °C) intended to promote the formation of embedded Si nanoparticles. The as-implanted state exhibits high densities of three prominent types of point defects, including the SiO₂-specific S and E'_γ O-vacancy type centers, and an unknown broad (≈20 G) signal at g ≈ 2.0026 denoted IS. The high-intensity S signal shows demagnetization shape effects, pointing to a distribution of high local density of defects over a thin layer. UST is observed to effectuate a drastic reduction in S and E'_γ centers, and elimination of IS beyond detection. This reveals a strong healing influence of *in situ* transferred ultrasound (US) energy on implantation-induced damage, here quantified and identified on atomic level in terms of mainly intrinsic paramagnetic point defects elimination, viz., Frenkel pair elimination, while all three initial signals disappear. Other types of defects surface after annealing of the non-US treated sample, including the SiO₂-specific EX defect signal and P_b-type Si/SiO₂ interface centers, the appearance of the latter providing direct ESR evidence for crystallization of the excess Si nanoparticles. The influence of the UST healing effect is kept up after subsequent annealing, now resulting in the absence of virtually all ESR-active centers. The drop in P_b-type centers below the detection level in the UST annealed sample indicates improvement of the nanocrystalline-Si/SiO₂ interface quality. The combination of UST with high-T annealing emerges as a highly efficient means to eradicate ion implantation damage in terms of intrinsic point defects. © 2010 American Institute of Physics. [doi:10.1063/1.3369041]

I. INTRODUCTION

The ability to tune the optical properties of silicon by controlling the size is a breakthrough achieved over the past two decades. In this, Si nanoparticles (np's) have received much interest, among others, because of the combination of adequate mechanical strength (when embedded in oxides) with good optical properties, thus paving the way to manufacturing of exceptional structures such as Si lasers and quantum computers,¹ with integration of optical components into the current Si-based semiconductor technology.² The Si np's are also introduced in complementary metal-oxide-semiconductor technology,^{3,4} flash memories,⁵ and photovoltaic applications.⁶ This makes the synthesis of Si np's of controlled size and particle/matrix interface quality of both fundamental and technological interest. Routinely, Si np's are embedded in SiO₂ as it enables realization of the high quality interface it naturally forms with Si. Recent work has demonstrated the possibility to control the origin of the photoluminescence between defects and quantum confinement in nanocrystalline (nc)-Si/SiO₂ entities obtained by the superlattice approach.⁷

For the fabrication of Si nc's embedded in SiO₂, the favored approach has Si-rich SiO₂ as starting material. The

oxides are typically annealed at 1100 °C for the excess Si to agglomerate and crystallize within the SiO₂ matrix. Implanting Si⁺ ions into a target oxide to increase the Si concentration above stoichiometric values is a preferred approach^{8,9} because of its easy integration into mass fabrication procedures, and other advantages such as easy masking methods, control of the implanted ion number, and penetration depth.¹⁰ One drawback, however, is the huge number of detrimental dangling bonds (DBs) introduced by the passage of the high-energy ions through the oxide: Bonds are being broken and part of the (displaced) ions is left not fully integrated into the network.

Ultrasonic stimulated processes in Si and Ge were discovered long ago and have been intensively explored over the past two decades.^{11,12} It is presently used in defect engineering to improve the performance and reliability of electronic devices.^{12,13} As interpreted, mechanical vibrations help atomic systems reach a better energetic state by increasing the mobility of interstitials and vacancies,¹⁴ decreasing the activation energy of point defect migration,^{13,15} and affecting the kinetics of point defects.^{16,17} The enhanced mobility of the interstitial atoms would lead to enhanced annihilation with vacancies, that is, removal of intrinsic point defects.¹³ The increased diffusion has also a beneficial effect on the nc nucleation and growth.^{11,16} Previous reports show that the effect of *in situ* applied ultrasound (US) during implantation

^{a)}Electronic mail: andre.stesmans@fys.kuleuven.be.

TABLE I. Treatments performed on (100)Si/SiO₂ structures with the SiO₂ layer implanted by 90 keV Si⁺ ions (8×10^{16} cm⁻²; 300 K). The UST was applied *in situ*.

Sample	UST frequency (MHz)	Anneal	
		Temperature (°C)	Time (min)
3K
4K
2KU	9.5
3Kan	...	1100	40
2KUan	9.5	1100	40

of SiO₂ with Cu or Ag ions lowers the precipitation threshold and increases cluster size.^{18,19} It may then come as a logical extension to study the influence of applying *in situ* ultrasound treatment (UST) during ion implantation in oxides in an attempt to affect (reduce) defect densities.

In view of the observed structural modification induced by the *in situ* applied US field, and the suggested role of intrinsic point defects in this effect, it would seem natural to attempt to extend experiments to analysis by electron spin resonance (ESR), a technique of choice for investigation and identification of point defects on atomic scale. Accordingly, in this work, we report on extensive ESR measurements carried out in the temperature range $T=4.2\text{--}300$ K to monitor and unveil on *atomic scale* the effect of *in situ* UST during Si⁺ ion implantation in thermal SiO₂. Using ESR, we effectively employ the unpaired electrons as local atomic “eyes,” sensing their surrounding. The UST effect is revealed here as impressively affecting (reducing) defect formation, both regarding defect types and changes in the densities: a main finding is the drastic reduction of O-vacancy type defects in the SiO₂ matrix. A detailed assessment in terms of the atomic nature of the various types of point defects involved is included.

II. EXPERIMENTAL DETAILS

A. Sample preparation

Investigated samples were obtained starting from growing 340-nm-thick thermal SiO₂ on 500- μ m-thick B-doped (100)Si wafers in dry oxygen at 1150 °C. Various samples were single side implanted [into the amorphous (a-) SiO₂ side] in one run at 300 K with 90 keV Si⁺ ions to a dose of 8×10^{16} cm⁻², without (reference samples 3K and 4K) or with (2KU) *in situ* subjection to 9.5 MHz UST (cf. Table I). for the entire duration of the implantation as reported elsewhere.¹⁸ For the ESR measurements, slices of 2×9 mm² main area were cut, where typically four were stacked in an ESR sample, forming a total implanted area not exceeding 0.72 mm². After protectively covering the implanted side, cutting and backside damage was removed through wet chemical etching (CP4). With the protective cover still on, slices were dipped in aqueous HF (5% HF in H₂O; 30 s) prior to each ESR measurement.

High-T annealing is used to enhance the mobility of Si atoms and their agglomeration into Si nc's embedded in

SiO₂. For this end, after initial ESR probing, pristine slices of samples 3K and 2KU were subjected to additional postimplantation annealing (PIA) at 1100 °C in N₂ for 40 min, resulting in the sets 3Kan and 2KUan, respectively. See Table I for an overview of the samples studied.

B. ESR spectroscopy

As the goal of this investigation is to trace and analyze, both qualitatively and quantitatively, the influence of *in situ* UST during the implantation process in terms of point defects involved, ESR is used as a tool able to provide information on the true atomic level through probing properties of the unpaired electron orbit of paramagnetic defects. ESR experiments were carried out in the range of 4.2–300 K using X, K, and Q band spectrometers, as outlined elsewhere.²⁰ Conventional continuous-wave (cw) first derivative-absorption (dP_{μ}/dB) spectra were measured through applying sinusoidal modulation (~ 100 kHz; amplitude $B_m \leq 0.8$ G) of the externally applied magnetic field **B**, with incident microwave power $P_{\mu} \leq 8 \times 10^{-10}$ W, i.e., cautiously reduced to avoid signal distortion.

The implantation process is creating a high density of defects, so the small amount of the investigated sample surface/volume does not prevent attaining good ESR sensitivity. However, that situation alters after annealing. The applied thermal budget results in a drastic decrease in the defect density and, consequently, signal-to-noise ratio has to be compensated by extensive signal averaging, typically raised now to $\sim 100\text{--}150$ scans. The relative error in defect density determination is limited (down to 3%–9%) by first computer simulating each ESR signal, including the one pertaining to an included reference sample, using known parameters such as line shape and g values from previously reported spectra. Absolute paramagnetic defect densities were determined through double numerical integration of the computer simulations by comparison, usually, of each signal to a co-mounted Si:P marker (electron spin $s=1/2$) with $g(4.2\text{ K}) = 1.998\,69 \pm 0.000\,02$ and $g(36\text{ K}) = 1.998\,78 \pm 0.000\,02$, or to a MgO:Mn marker ($s=5/2$; nuclear spin $I=5/2$) in the case of X-band room temperature (RT) measurements.

C. Sample morphology

To assess changes in the morphology, the samples with and without applied US were investigated after high-temperature annealing by cross-sectional high resolution transmission electron microscopy (HRTEM), showing the presence of Si nanocrystallites, as more detailed elsewhere.²¹ From analysis of bright field HRTEM images, the average Si np size was inferred as 1.92 ± 0.7 and 1.97 ± 0.7 nm for the annealed reference and UST samples, respectively, that is, very close, indeed. The analysis of dark-field TEM images indicates that the depth distribution profile of Si np's is much similar, with the centroid at ~ 130 nm, close to the Si implantation projected range.

Using the SRIM code,²² simulation of the implanted Si⁺ atom distribution in the a-SiO₂ layer gave a peak implantation depth of ~ 134 nm with half-height width of ~ 89 nm. Importantly, no implantation damage of the remote

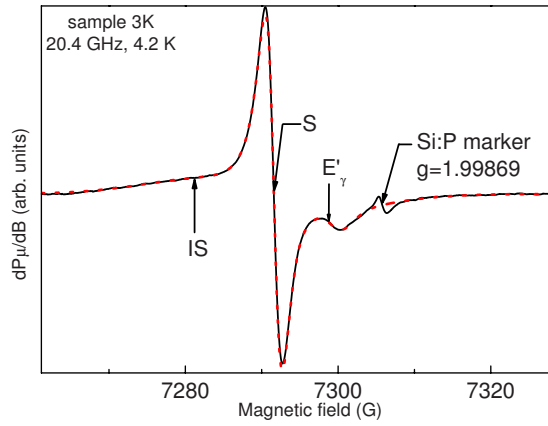


FIG. 1. (Color online) cw low power first harmonic K-band spectrum taken on sample 3K at 4.2 K for $\varphi_B=55^\circ$ using $P_\mu \approx 8 \times 10^{-10}$ W and $B_m \approx 0.5$ G. An intense spectrum is observed (solid trace) composed of three types of signals, marked as S, E'_γ , and IS. The signal at $g_c=1.998\,69$ stems from a comounted Si:P marker sample. The dashed curve represents an optimized spectral fitting based on the powder pattern approach and known spectral properties of the resolved signals (defects).

substrate-Si/SiO₂ interface would have occurred.

The details provided by ESR about the actual location of paramagnetic centers in the implanted SiO₂ matrix, their density, and presence of demagnetization features may also appear all valuable in deriving morphological properties. Information about the nc-Si/SiO₂ interface orientations can tentatively be assessed with the help of ESR active P_b-type interface defects, as discussed later.

III. RESULTS AND ANALYSIS

A. Paramagnetic defects in reference samples

Figure 1 shows a typical K-band spectrum observed for $\varphi_B=55^\circ$ (the field angle of \mathbf{B} with \mathbf{n} , the [100] Si substrate normal) on reference sample 3K, revealing the presence of various types of signals (defects). Apart from the Si:P signal, three different signals may be distinguished. Starting from the high field side, the signal closest to the marker, based on its zero crossing g value $g_c=2.000\,55$ and specific signal shape, unmistakably originates from the E'_γ center²³ (generic entity $O_3 \equiv Si^*$; an unpaired electron localized in an sp^3 -like orbital on a Si atom backbonded to three oxygen atoms); the identification is further supported by the observation of the 434 G associated ²⁹Si hyperfine (hf) doublet^{24,25} (not shown here). The inferred density amounts to $[E'_\gamma]=(2.8 \pm 0.1) \times 10^{14}$ cm⁻².

Second, we observe an intense rather narrow symmetric signal of Lorentzian shape with peak-to-peak width $\Delta B_{pp}=2.3 \pm 0.2$ G and corresponding density of $(2.9 \pm 0.2) \times 10^{15}$ cm⁻². Assuming the originating centers to be uniformly distributed over an 89 nm thick layer as obtained from SRIM calculation, this gives a high volumetric density $N_V \approx 3 \times 10^{20}$ cm⁻³. As the ESR study concerns defects residing in an amorphous SiO₂ matrix, one would routinely expect the observation of “isotropic” or powder pattern line shapes. Yet, angular measurements for changing field angle φ_B and T-dependent study indicated the g_c of this signal (unlike the other signals observed) to exhibit a specific field

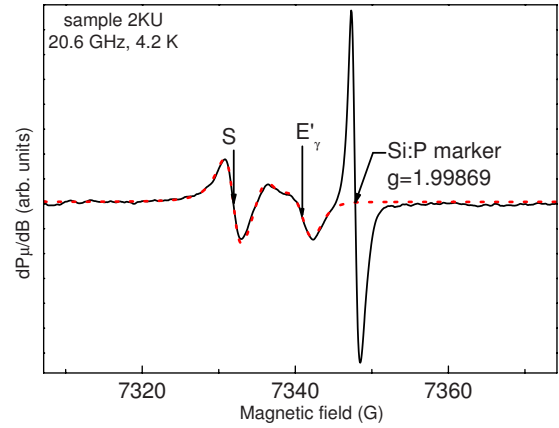


FIG. 2. (Color online) A representative low power first harmonic K-band spectrum measured on sample 2KU at 4.2 K for $\mathbf{B} \perp \mathbf{n}$. Only S and E'_γ center signals are observed in this case. The dashed curve represents an optimized spectral fitting.

anisotropy that asymptotically vanishes towards high-T. The φ_B -independent reference value of g_c (g_{ref}) is obtained (vide infra) from RT X-band spectrometry as $g_{ref}=2.002\,52 \pm 0.000\,05$. As detailed later, we assign this signal to S centers ($SiO_2 \equiv Si^*$),^{26–28} characteristic for Si-enriched SiO₂. In Fig. 1 this signal is noticed to be slightly asymmetric due to a slight g matrix anisotropy, as reported before.²⁰

Finally, the broad isotropic signal, extending over almost the whole spectrum, could be accurately simulated using a Gaussian line shape of $\Delta B_{pp}=20.0 \pm 0.4$ G centered at $g_c=2.0026 \pm 0.0001$, resulting in a density of $(4.2 \pm 0.4) \times 10^{15}$ cm⁻². No previous report of such signal could be traced in the literature. The signal is labeled as IS (implantation induced signal).

K-band measurements performed on sample 4K gave very similar results as sample 3K. All three types of centers are present in the same ratios (within the experimental error), indicating that the implantation method is reproducible in terms of induced paramagnetic defects.

B. Influence of UST on as-implanted samples

Figure 2 shows a K-band spectrum observed at 4.2 K for $\mathbf{B} \perp \mathbf{n}$ on the 2KU sample *in situ* treated by US during Si⁺ implantation. Only the two signals corresponding to S and E'_γ centers remain visible here. Compared with the 3K reference sample (Fig. 1), a drastic decrease, by ~ 60 times, in total number (signal) of defects is noticed, i.e., from $(7.3 \pm 0.5) \times 10^{15}$ cm⁻² for 3K to $(1.2 \pm 0.1) \times 10^{14}$ cm⁻² for 2KU, cf. Figs. 1 and 2 where the same marker was used and about equal sample area. The IS signal is seen to drop below the detection limit.

The evolution of defect density with different treatments is pictured in Fig. 3 to better expose the UST impact. Left and right parts correspond to the as-received and annealed samples, respectively. The lines guide the eye. The *in situ* UST applied during implantation is thus found to ensue a drastic effect on the defect densities in the sense of improving sample quality.

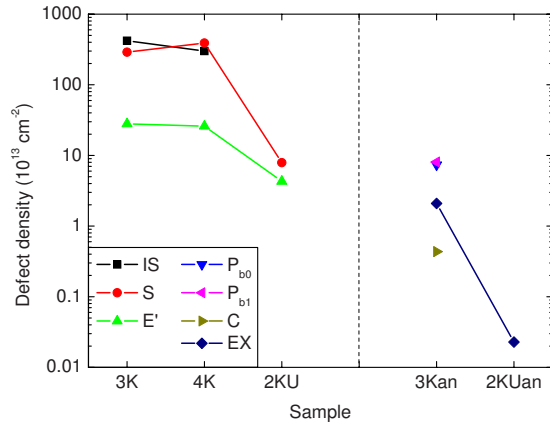


FIG. 3. (Color online) Inferred areal densities of the paramagnetic centers resolved in the as-implanted and annealed samples, both with and without UST application during implantation. The graph clearly shows the drastic impact of *in situ* UST in decreasing defect numbers, an effect maintained also after annealing. Error bars are within the size of the symbols.

C. Magnetism of S centers

The kind of magnetic behavior of the S defects was investigated by measuring the ESR intensity I (area under the absorption curve) $\propto \chi$, where χ is the magnetic susceptibility, as a function of T in the range of 4.2–36 K for $\mathbf{B} \parallel \mathbf{n}$. The data, shown in Fig. 4 for sample 4K as a $1/\chi$ -versus- T plot, indicate a Currie–Weiss type behavior, i.e.,

$$\chi = \frac{C}{T - T_C} = \frac{\mu_0 N_V g_c^2 \beta^2 s(s+1)}{3k_B(T - T_C)}, \quad (1)$$

where μ_0 is the free space magnetic permeability, β the Bohr magneton, s the defect spin, k_B the Boltzmann constant, T_C the Currie temperature, and C the Currie constant, proportional to the volumetric spin density N_V . Optimized fitting of Eq. (1) gives $T_C = 0 \pm 1$ K, pointing to a purely paramagnetic system comprised of negligibly interacting magnetic moments (defects).

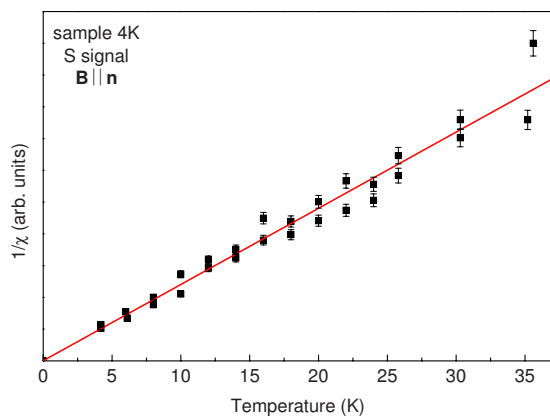


FIG. 4. (Color online) Temperature dependence of the intrinsic ESR intensity I ($\propto \chi$) of the S signal measured in the sample 4K for $\mathbf{B} \parallel \mathbf{n}$ (K-band data). The solid line represents a fit of Eq. (1), from where a Currie temperature $T_C = 0 \pm 1$ K is inferred, pointing to a close Currie-type susceptibility behavior.

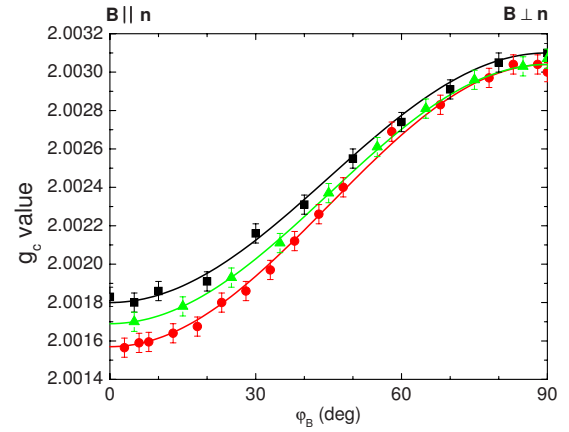


FIG. 5. (Color online) Anisotropy of the S center g_c value as a function of the magnet angle φ_B as measured by K-band ESR at 4.2 K on samples 3K (\blacktriangle), 4K (\blacksquare), and 2KU (\bullet). The solid lines represent simulations using Eq. (2). The g shift arises from demagnetization (shape effect) for a system of defects of high local density residing within a thin layer.

D. Demagnetization effects

Commonly, no anisotropic (φ_B dependent) ESR signals are expected from ion-implanted a-SiO₂. However, such anisotropy was observed in the case of the S signal, yet not for the IS and E'_γ signals. The anisotropy could readily be traced down as originating from demagnetization effects (a sample shape effect) indicating the signal to stem from a *large* local density of defects in a planar (thin film) arrangement, consistent with the inferred large areal density (here $> 4 \times 10^{15} \text{ cm}^{-2}$) in combination with the limited Si⁺ implantation depth. The effect is only observed on as-implanted samples showing a very intense S-signal—but not after annealing. Figure 5 depicts the dependence of g_c on φ_B (relative accuracy of $\approx 0.5^\circ$) as obtained from K-band (4.2 K) spectra for the three investigated unannealed samples. For example, in the case of sample 3K, g_c (4.2 K) is seen to evolve between 2.00170 ± 0.00005 ($\mathbf{B} \parallel \mathbf{n}$) and 2.00307 ± 0.00005 ($\mathbf{B} \perp \mathbf{n}$), definitely well beyond experimental error. A slight decrease in ΔB_{pp} with increasing φ_B of ≈ 0.4 G was also observed, that is from $\Delta B_{pp}(\varphi_B = 0^\circ) \approx 2.5$ G to $\Delta B_{pp}(\varphi_B = 90^\circ) \approx 2.1$ G.

Figure 6 shows the extreme g values, g_{\parallel} and g_{\perp} , as a

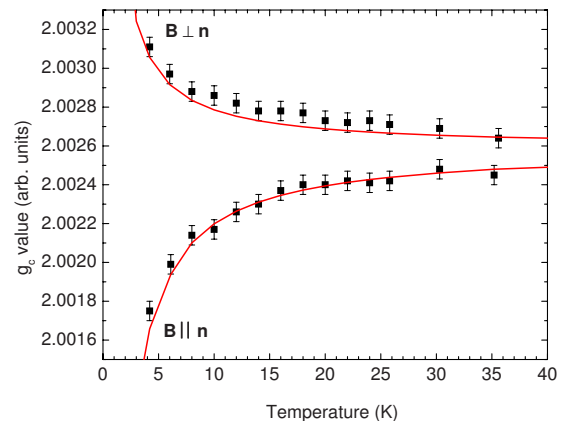


FIG. 6. (Color online) Evolution as a function of T of the extreme g_c values of the S signal obtained at K-band for $\mathbf{B} \parallel \mathbf{n}$ and $\mathbf{B} \perp \mathbf{n}$ on sample 4K. The solid curves represent optimized fittings based on Eqs. (1) and (3).

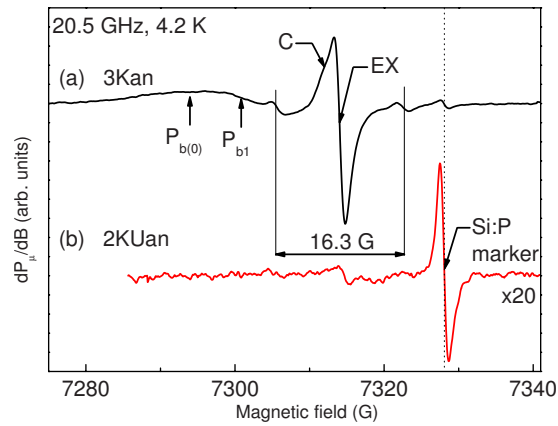


FIG. 7. (Color online) Specific K-band spectra taken at 4.2 K ($B_m \leq 0.6$ G; $P_\mu \approx 3 \times 10^{-10}$ W) on the annealed samples 3Kan and 2KUan (1100 °C; 40 min; N_2). The $P_{b(0)}$ and P_{b1} signals indicate nc-Si formation. Only a weak EX signal remains observable for the UST sample.

function of T in the range of 4.2–36 K for sample 4K, the one exhibiting the most pronounced anisotropy of all. It is obvious from this figure that both extremes tend to merge into a singular value at higher temperatures with attendant vanishing of the g anisotropy. The angular anisotropy is found to be suppressed in RT X-band spectra: a Lorentzian isotropic signal is observed with $\Delta B_{pp} = 2.2 \pm 0.1$ G giving for g_c the reference value $g_{ref} = 2.002\,52 \pm 0.000\,05$ unaffected by demagnetization.

E. Annealed samples

The effect of PIA (1100 °C; N_2) has been investigated with the view to trace any possible correlation of the initial implantation induced point defect damage with the post-anneal result. Figure 7 shows (top curve) a K-band spectrum observed at 4.2 K on sample 3Kan. As expected, compared with the unannealed state (Fig. 1), the ESR spectrum has substantially changed with all three previous signals— E'_γ , S , and IS —being eliminated beyond detection. Computer-assisted spectral disentanglement now, instead, indicates the presence of (at least) four types of other defects, albeit with an overall much reduced densities. Two pertain to the Si/SiO₂ interface, namely, P_b and/or P_{b0} , and P_{b1} , in almost equal quantities, summing to $(1.5 \pm 0.1) \times 10^{14}$ cm⁻², and indicating that nc-Si particles have been formed²⁹ within the a-SiO₂ matrix during the postmanufacturing anneal. The observed responses exhibit powder pattern line shapes, and were simulated that way, using known principal g values, showing no B direction anisotropy.

Briefly, the P_b -type defects, invariably introduced at the Si/SiO₂ interface as a result of lattice-network mismatch,^{30–33} correlate with interface orientation in registry with the crystallinity of the Si. At the (111)Si/SiO₂ interface, the only type observed—specifically termed P_b —was identified as trivalent interfacial Si ($Si_3 \equiv Si^\bullet$, where the dot represents an unpaired electron in a dangling Si sp^3 hybrid) backbonded to three Si atoms in the bulk. The technologically favored (100)Si/SiO₂ interface exhibits two types, termed P_{b0} and P_{b1} . The experimental evidence is that P_{b0} is chemically identical to P_b , but now residing at microscopically

(111)-oriented Si/SiO₂ facets. The P_{b1} center is assigned to a distorted defected interfacial Si–Si dimer ($a \equiv Si-Si^\bullet=Si_2$ defect, where the endash symbolizes a strained bond, with an approximately $\langle 211 \rangle$ oriented unpaired Si sp^3 hybrid).³⁴ At the (110)Si/SiO₂ interface also, only one type, the P_b variant, is observed.^{32,35} Thus all three types were shown to be interfacial trivalent Si centers,³⁵ naturally occurring for standard oxidation temperatures (800–960 °C) in areal densities of $[P_b] \approx 5 \times 10^{12}$ cm⁻² (Refs. 31 and 36–38) and $[P_{b0}]$, $[P_{b1}] \approx 1 \times 10^{12}$ cm⁻² (Ref. 36).

Besides the interface specific signals, an intrinsic a-SiO₂ center emerges at $g_c = 2.002\,55 \pm 0.000\,2$, i.e., the EX defect, with density $\approx 2.1 \times 10^{13}$ cm⁻² as confirmed by the observation of its characteristic 16.3 G split hf doublet. A fourth signal at $g_c = 2.003\,00 \pm 0.000\,03$, with corresponding density of $(4.6 \pm 0.8) \times 10^{12}$ cm⁻², is ascribed to C impurities^{39–41} in SiO₂, a contaminant probably introduced during implantation.

By contrast, a much noteworthy observation is that, as illustrated in Fig. 7 (bottom spectrum), only a faint EX signal remains as sole ESR relic in the US-treated sample after annealing, 2KUan, about two orders of magnitude smaller than for the 3Kan reference sample. As the two samples were physically annealed together in the same step, it points to the *in situ* UST as the decisive factor of difference. This, interestingly, reveals the combination of *in situ* US treatment with post implantation high-T annealing as a process resulting in virtually the entire removal (prevention) of paramagnetic point defects beyond the ESR sensitivity limit.

IV. INTERPRETATION AND DISCUSSION

A. As-implanted samples

The K-band ESR spectra measured at 4.2 K on the reference samples 3K (cf. Fig. 1) and 4K are similar, so we will restrict the discussion to 3K data unless specified otherwise. In the as-implanted reference samples three paramagnetic defects are observed by ESR. The signal closest to the marker, as indicated in Fig. 1, is assigned to the a-SiO₂ specific E'_γ point defect based on the specific double peak powder pattern shape and the $g_c = 2.000\,55$ value⁴¹ of the signal. This point defect is envisioned^{42,43} as an unpaired Si sp^3 hybrid on a Si atom backbonded to three O atoms at the site of an O vacancy. It can be used as an indication of the oxide quality, the typical value⁴⁴ for standard thermally grown SiO₂ on Si substrate being $\sim 3 \times 10^{17}$ m⁻³. The measured density in the case of our reference samples, with a SiO₂ layer of 340 nm thick, is $(8.3 \pm 0.2) \times 10^{18}$ cm⁻³, indicating that indeed the matrix is degraded by the implantation. For this center we also measured in Q band at ≈ 10 K the principal hf doublet arising from central ²⁹Si isotopes⁴⁵ (4.7% natural abundance; $I = 1/2$). Its splitting of 434 ± 2 G is found to be larger than the standard value of 420 G reported for bulk silica glasses.^{45,46} This increased hf splitting has been explained before^{25,47} as a consequence of SiO₂ matrix densification, here effectuated by Si⁺ ion implantation, resulting in an increase of the average bond angle between the Si DB direction and the Si back bonds to O (see Ref. 47 and references therein).

Most prominent in the ESR spectrum is the sharp intense central signal of Lorentzian line shape. This signal sweeps a spectral region between $g_{\parallel} \approx 2.0016$ and $g_{\perp} = 2.0031$ with varying φ_B (see Fig. 5), an unexpected behavior since the as-implanted samples under investigation are amorphous and the interface with the Si substrate is not reached by the implanted Si^+ ions as evident from SRIM simulations. It results from demagnetization effects, as detailed before. On the basis of the inferred g_{ref} , obvious SiO_2 -associated defect candidates include the EX center, with g_c values reported between^{48,49} 2.002 47 and 2.0027, and the S center^{26–28,50} with^{20,27,28} $g = 2.0027 \pm 0.0001$ attributed to⁵¹ the $n=1$ variant of the $\text{Si}_n\text{O}_{3-n} \equiv \text{Si}^*$ ($n=1,2$) type centers intermediate^{25,26} between a-SiO_2 -specific E'_{γ} defects⁴³ ($\text{O}_3 \equiv \text{Si}^*$) and the P_b center ($\text{Si}_3 \equiv \text{Si}^*$), the archetypal (111)Si/SiO₂ interface defect.^{30–33,52} In a preliminary model, the EX center has been pictured as a hole delocalized over four oxygen atoms formally at the site of a Si vacancy;⁴⁸ in another view it can also be looked at as an agglomerate of four oxygen-related hole centers. Although the “morphology” of S and EX signals is distinct, their g_c values are close. So, additional information will be needed, e.g., hf splitting, for correct assignment. Generally, the spectra of both types of defects considered include a ^{29}Si associated hf doublet. In the case of EX centers a 16.1 G hf doublet⁵³ has been reported of which an example can be seen in Fig. 7 (top curve) measured on the *annealed* sample 3Kan. As to the S center, two (^{29}Si) hf doublets, of splitting ≈ 162 and 289 G, have been reported where over the various reports the latter one appears to fluctuate^{20,25,50,54} between 230 and 289 G. Yet, no doublet centered at $g \approx 2.0025$ could be measured for any of the as-implanted samples. This may be explained by the strong wave function overlap at high defect concentrations, the signals being exchanged narrowed (see, e.g., Refs. 55 and 56) leading to the “collapse” of the hf lines into the central signal (vide infra). This is likely the case here, where the estimated volume density exceeds $3 \times 10^{20} \text{ cm}^{-3}$. So, no additional (^{29}Si) hf structure for this signal could be resolved, which in addition with the featureless shape makes defect identification difficult. The excess of Si introduced by implantation makes us incline toward one or a mixture of the intermediate $\text{Si}_n\text{O}_{3-n} \equiv \text{Si}^*$ ($n=1,2$) type centers, labeled as X ($n=1$) and Y ($n=2$) centers in some works.^{50,57,58}

The spectrum in Fig. 1 is overlapped by an isotropic Gaussian signal of $\Delta B_{\text{pp}} = 20 \pm 0.4$ G, centered at $g_c = 2.0026 \pm 0.0001$. The origin of this signal remains so far unknown. Being an implantation induced signal, we labeled it IS. Although the density of IS centers (cf. Fig. 3) is comparable to that of S centers, no demagnetization effects could be noticed, indicating then a broader depth distribution over the oxide, i.e., a lower local volumetric density.

For completeness, we mention the inferred defect densities for the other reference sample, 4K. These are given as $[\text{IS}] = (3.0 \pm 0.1) \times 10^{15} \text{ cm}^{-2}$, $[\text{S}] = (3.9 \pm 0.1) \times 10^{15} \text{ cm}^{-2}$, and $[\text{E}'_{\gamma}] = (2.6 \pm 0.1) \times 10^{14} \text{ cm}^{-2}$, i.e., in the same range as the respective densities for the sample 3K, indicating a reproducible implantation process in terms of point defects.

B. Demagnetization

As noticed before, Fig. 5 reveals the remarkable observation that for all as-implanted samples, the g_c value of the main ESR signal (cf. Figs. 1 and 2) is dependent on φ_B . Yet, as it is attributed to S centers in $\text{a-SiO}_{2(x)}$, that is, an amorphous material, microscopic defect anisotropy like, e.g., due to g anisotropy will be averaged out orientationally. So, the response—a powder pattern—should be isotropic. As illustrated by the full curves, the experimental values, varying between g_{\parallel} and g_{\perp} , can be well fitted by

$$g_c = \sqrt{(g_{\parallel} \cos \phi_B)^2 + (g_{\perp} \sin \phi_B)^2}, \quad (2)$$

describing the g anisotropy for an axial symmetric (interface) defect. This axial symmetry, though, is only seeming as it is seen to disappear for increasing T (see Fig. 6). Rather, as mentioned before, it stems from an “artifact,” i.e., spatial defect distribution dependent demagnetization—more precisely, due to a macroscopic (sample) shape effect. Demagnetization effects on physical properties are well known, such as in relation with ferromagnetic and superconducting matter.^{59–62} Its impact and appearance is set by a combination of applied magnetic field direction, sample, shape, and magnetization. Anisotropic demagnetization is characteristic to magnetic samples of irregular shape put in a uniform magnetic field \mathbf{B} . The nonuniform surrounding results in an effective (local) field dependent on the direction of \mathbf{B} , emerging, e.g., in ESR, as angle dependent g_c values.

The main, most direct, hint to the influence of demagnetization comes from the g_c -versus- T plot (Fig. 6), pictured in the current case as arising from a system of paramagnetic defects densely packed over a thin layer, i.e., a disk-shaped sample configuration. For such elemental case, for $\chi(T) \ll 1$, the effect is found to result in (Système International units)²⁰

$$g_c(T) = \begin{cases} g_{\text{ref}}[1 + 0.5\chi(T)] & \text{for } \mathbf{B} \perp \mathbf{n} \\ g_{\text{ref}}[1 - \chi(T)] & \text{for } \mathbf{B} \parallel \mathbf{n}. \end{cases} \quad (3)$$

Combining Eqs. (1) and (3) (taking $T_C=0$, as inferred above) results in self-consistent successful fitting (curves in Fig. 6) of the T dependence of g_c for both field orientations, from where the values $g_{\text{ref}} = 2.00259 \pm 0.00005$ and $N_V = (2.6 \pm 0.2) \times 10^{20} \text{ cm}^{-3}$ are inferred. While the former value is in accordance with the direct RT X-band result, the later is consistent with the value ($\approx 3 \times 10^{20} \text{ cm}^{-3}$) obtained from direct ESR defect density measurements and the SRIM width (~ 89 nm), demonstrating internal consistency.

At such an elevated unpaired electron concentration, the mutual defect interaction is no longer negligible. In the case of randomly distributed diluted centers of spin $s=1/2$, when less than 1% of the lattice sites⁶³ have an unpaired electron, as S centers here, dipolar interaction causes a (cutoff) Lorentzian line shape broadening of width^{64,65}

$$\Delta B_{\text{pp}}(\text{G}) = 0.54 \times 10^{-19} \times N_V(\text{cm}^{-3}), \quad (4)$$

where a factor of 2/3 has been incorporated to account for (evidenced) g anisotropy.⁶⁴ Accordingly, the above encountered N_V value would entail a dipolar linewidth contribution of ≈ 14 G, significantly larger (~ 5 times) than that of the intrinsic S signal ($\Delta B_{\text{pp}} \approx 2.6$ G) previously reported⁶⁶ for

diluted systems and clearly unlike the narrow signals ($\Delta B_{pp} \approx 2.1\text{--}2.5$ G) currently observed as well. Yet, at high local spin densities, exchange interactions narrow the resonance response toward the apparent width^{67,68} $\Delta\omega = \omega_p^2 / \omega_e$, where ω_p is the root-mean-square of the dipolar perturbation and ω_e the exchange narrowing, all in frequency units. If sufficiently rapid, the exchange-induced interactions *inhomogeneously* average out the dipolar field seen by a spin⁶⁹ resulting in a Lorentzian⁶³ line shape. Movaghar *et al.*⁶⁵ showed that for a density of $\sim 10^{20}$ cm⁻³ D centers⁷⁰ in a-Si the exchange interaction prevails, completely narrowing down dipolar and hf interactions. Obviously, as we are dealing with defect densities $N_V \approx 2.6 \times 10^{20}$ cm⁻³, it is clear that exchange narrowing may well account for the observed narrow S signal of Lorentzian shape with collapsed hf structure.

As can be seen from Fig. 5, all three as-implanted samples exhibit almost equal Δg_c values, thus suggesting similar values for N_V , although [S] is found to be drastically lower in sample 2KU. This would indicate the S centers to be distributed over a thinner layer as a result of the UST compared with the untreated samples.

C. Influence of UST

The previous paragraphs have made it clear that, as expected, the densities of intrinsic paramagnetic defects are very high in the as-implanted reference samples. It is a general main drawback of the bare implantation technique, otherwise much versatile to increase the Si density in SiO₂. Reduction (elimination) of implantation damage has been the subject of intense research in various solid state fields, such as, e.g., semiconductor technologies.^{13,15,17} In fact, the main objective of the current research is to evaluate the application of *in situ* UST as a method of suppressing implantation damage. Studying the influence of US on the ionic diffusion process in semiconductors, Krevchik *et al.*¹⁵ concluded that the acoustic field disturbs the equilibrium state of the phonon subsystem, resulting in an energy exchange between non-equilibrium phonons and impurity atoms, thus decreasing the activation energy for impurity migration. Improved migration was also found by Franklin and Sengupta¹⁷ using stimulated Raman scattering and IR absorption measurements. Furthermore, Ostapenko¹³ found that UST applied to hydrogenated Si-based thin films is beneficial in improving defect recombination (annihilation) and transport characteristics of implanted species.

In the current work on the analysis of point defect generation, the superb positive healing effect of *in situ* UST during Si⁺ implantation is immediately evident from comparing Figs. 1 and 2, showing the ESR spectra measured on samples without or with UST applied, respectively (same Si:P marker used for both spectra). Applying UST is seen to result in a ≈ 43 times decrease in [S], ≈ 6 times decrease in $[E'_\gamma]$, while IS is suppressed below the sensitivity limit (cf. Fig. 3). While UST appears not equally efficient for all three types of ESR centers, the effect is impressive, confirming the drastic impact of nonequilibrium phonons on implanted species and attendant generated point defects. In particular, we

note the influence on two of the main types of defects resolved, E'_γ and S center, which, as modeled, both essentially concern O-vacancy type centers: the drastic effect of UST on the occurrence of these centers, here clearly exposed by ESR to atomic detail, thus supports previous modeling^{14,15} where, in essence, enhanced mobility of displaced atoms will result in enhanced elimination of vacancies (Frenkel pairs).

There is one more noteworthy observation: although the S centers density is decreased about 43 times as a result of applying UST, the ESR signal still remains affected by demagnetization to a much similar extent. The net effect seems that, as a result of *in situ* UST, the defects are partially annihilated while the remaining gather into a thinner layer.

D. Influence of annealing

The ESR measurements on sample 3Kan, annealed at 1100 °C, show the presence of signals ($P_{b(0)}$, P_{b1}) typical²⁹ for nc-Si embedded in a-SiO₂ matrix. The powder pattern signals, showing up in the low field part of spectrum in Fig. 7 (top curve), pertain to Si DBs of P_b -type defects, the well known interface point defects in thermal Si/SiO₂. Here, we should add that since P_b and P_{b0} basically concern the same Si DB defect (close g matrices and linewidth), but pertaining at different interfaces, i.e., (111)Si/SiO₂ and (100)Si/SiO₂, respectively, their powder patterns are much similar. This makes undubious distinction difficult from where the signal is denoted as $P_{b(0)}$.

As mentioned, P_b -type defects correlate with the Si/SiO₂ interface orientation, leading to field angle dependent signals (anisotropy). The fact then that the signals are powder patterns indicates that the nc-Si/SiO₂ interfaces are randomly oriented, as might be expected for the amorphous matrix cannot instigate a *common* crystalline orientation for the crystallites grown in it.

Noteworthy is that, despite intensively searched for under various directions of **B**, there appears within experimental accuracy no evidence of D centers,⁷¹ Si DBs in an a-Si environment. This would indicate that of all Si np's formed in the SiO_{2(x)} matrix, none, or only a negligible fraction, might have been left in the amorphous state. So, most, if not all, are crystalline.

Since the number of the embedded Si particles is not known from independent measurements, no further conclusions on occurring number of interface defects per Si particle can be drawn. Previous ESR measurements²⁹ on nc-Si embedded in SiO₂ obtained by high-T annealing (same as here) of SiO/SiO₂ superlattices found a closely one-to-one P_b -type defect-per-Si nc ratio. Assuming a similar nc-Si/SiO₂ interface quality in the current case, we can estimate the order of Si nc's created at $\sim 10^{14}$ cm⁻².

Finally, there is the signal ascribed to C impurities observed in sample 3Kan. This would mean that contamination occurred in the as-grown state or introduced during subsequent annealing. But if sample 3Kan would have been contaminated by high-T annealing, sample 2KUan should exhibit the C signal in a comparable density as well since the two samples have been annealed physically together. Yet, as the latter sample shows no C signal but only a weak EX

signal $[(EX) = (2.3 \pm 0.1) \times 10^{11} \text{ cm}^{-2}]$, we conclude that this impurification concerns a side effect of the implantation process.

The influence of *in situ* UST is stunning when comparing samples 3Kan and 2KUan. For sample 2KUan only a faint EX signal remains and no P_b -type defects (cf. Fig. 7). Considering that the two samples were annealed together, it would bear out the application of the *in situ* UST during Si^+ ion implantation as the only matter of difference. We also note that combination of UST with postimplantation high-T annealing (1100°C ; 1 atm in N_2) almost results in the removal of virtually all ESR-active defects beyond the detection level.

V. SUMMARY AND CONCLUSIONS

A multifrequency ESR study has been carried out on the effect of *in situ* applied 9.5 MHz US excitation during the implantation of the SiO_2 layer of (100)Si/ SiO_2 entities with 90 keV Si^+ ions. The UST, which is applied to promote Si np nucleation and growth, has been found successful in previous work on Cu and Ag implantation, where the effect was attributed to enhanced diffusion of generated interstitials as a result of energy exchange with the defect system.

For the as-implanted state, significant densities of three types of paramagnetic centers are resolved including the well known E'_γ , a signal at g_{ref} (X-band) 2.002 52 ascribed to S centers ($\text{Si}_n\text{O}_{3-n} \equiv \text{Si}^+$; $n=1, 2$), and an unknown signal, denoted IS, at $g_c \approx 2.0026$; the latter two, of comparable intensity, are the most intense, about $10 \times$ larger than $[E'_\gamma]$. As modeled, both E'_γ and S centers are O-vacancy-type defects. The high-intensity S signal is observed to show demagnetization effects (field angle dependent g_c shift) characteristic for a disklike sample shape. It points to an arrangement of a high local density of paramagnetic species over a thin layer, not unexpected for ion implantation damage in an insulator; a local density of $\approx 3 \times 10^{20} \text{ cm}^{-3}$ is inferred. The signal susceptibility shows a closely Currie-type behavior with $T_C = 0 \pm 1 \text{ K}$.

On the basis of the paramagnetic defect criterion, the *in situ* UST is found to effectuate a substantial beneficial influence, that is, a drastic reduction in S and E'_γ centers (~ 43 and ~ 6 times, respectively), with elimination of IS beyond detection: UST establishes an impressive healing effect, here demonstrated quantitatively, by *in situ* furnishing of nonequilibrium megahertz phonons. It provides atomic evidence for previous modeling where, in essence, the US activation would, via the modified phonon system, give rise to enhanced mobility of displaced atoms with enhanced annihilation of *vacancies* as a result.

As expected, postimplantation high-T ($\approx 1100^\circ\text{C}$) annealing, intended to form embedded Si np's, ensued a substantial defect repairing effect, with elimination of the three dominant types of defects (E'_γ , S, and IS) beyond ESR detection. Instead, four other types of signals, albeit in much lower (orders of magnitude) density, emerge including the P_b -type Si/ SiO_2 interface centers, EX, and a weak component ascribed to C impurification. Next, combination of UST with PIA is found to result in removal of virtually all ESR-

active centers ($\approx 2 \times 10^{11} \text{ cm}^{-2}$), with only a faint EX signal remaining. The beneficial influence of UST is thus found retained after additional high-T annealing: combination of *in situ* UST with postimplantation high-T annealing emerges as a highly efficient means to remove/prevent implantation damage in terms of intrinsic point defects.

- ¹L. Pavesi, *J. Phys.: Condens. Matter* **15**, R1169 (2003).
- ²G. G. Ross, D. Barba, and F. Martin, *Int. J. Nanotechnol.* **5**, 984 (2008).
- ³M. Porti, M. Avidano, M. Nafria, X. Aymerich, J. Carreras, O. Jambois, and B. Garrido, *J. Appl. Phys.* **101**, 064509 (2007).
- ⁴K. I. Han, Y. M. Park, S. Kim, S. H. Choi, K. J. Kim, I. H. Park, and B. G. Park, *IEEE Trans. Electron Devices* **54**, 359 (2007).
- ⁵T. Z. Lu, J. Shen, B. Mereu, M. Alexe, R. Scholz, V. Talalaev, and M. Zacharias, *Appl. Phys. A: Mater. Sci. Process.* **80**, 1631 (2005).
- ⁶S. Pizzini, M. Acciarri, S. Binetti, D. Cavalcoli, A. Cavallini, D. Chrastina, L. Colombo, E. Grilli, G. Isella, M. Lancini, A. Le Donne, A. Mattoni, K. Peter, B. Pichaud, E. Poliani, M. Rossi, S. Sanguinetti, M. Texier, and H. von Kanel, *Mater. Sci. Eng., B* **134**, 118 (2006).
- ⁷S. Godefroo, M. Hayne, M. Jivanescu, A. Stesmans, M. Zacharias, O. I. Lebedev, G. Van Tendeloo, and V. V. Moshchalkov, *Nat. Nanotechnol.* **3**, 174 (2008).
- ⁸V. Levitcharsky, R. G. Saint-Jacques, Y. Q. Wang, L. Nikolova, R. Smirani, and G. G. Ross, *Surf. Coat. Technol.* **201**, 8547 (2007).
- ⁹T. Shimizu-Iwayama, D. E. Hole, and P. D. Townsend, *J. Lumin.* **80**, 235 (1998).
- ¹⁰S. Dhara, *Crit. Rev. Solid State Mater. Sci.* **32**, 1 (2007).
- ¹¹I. V. Ostrovskii and V. N. Lysenko, *Sov. Phys. Solid State* **24**, 682 (1982).
- ¹²S. Ostapenko, N. E. Korsunskaya, M. K. Sheinkman, and S. V. Koveshnikov, *Encyclopedia of Electrical and Electronics Engineering* (Wiley, New York, 1999).
- ¹³S. Ostapenko, *Appl. Phys. A: Mater. Sci. Process.* **69**, 225 (1999).
- ¹⁴D. Krüger, B. Romanyuk, V. Melnik, Y. Olikh, and R. Kurps, *J. Vac. Sci. Technol. B* **20**, 1448 (2002).
- ¹⁵V. D. Krevchik, R. A. Muminov, and A. Y. Yafasov, *Phys. Status Solidi A* **63**, K159 (1981).
- ¹⁶V. N. Pavlovich, *Phys. Status Solidi B* **180**, 97 (1993).
- ¹⁷W. M. Franklin and P. Sengupta, *IEEE J. Quantum Electron.* **8**, 393 (1972).
- ¹⁸A. Romanyuk, V. Spassov, and V. Melnik, *J. Appl. Phys.* **99**, 034314 (2006).
- ¹⁹A. Romanyuk, P. Oelhafen, R. Kurps, and V. Melnik, *Appl. Phys. Lett.* **90**, 013118 (2007).
- ²⁰A. Stesmans, B. Nouwen, and V. V. Afanas'ev, *Phys. Rev. B* **66**, 045307 (2002).
- ²¹A. Romanyuk, V. Melnik, Y. Olikh, J. Biskupek, U. Kaiser, M. Feneberg, K. Thonke, and P. Oelhafen, *J. Lumin.* **130**, 87 (2010).
- ²²<http://www.srim.org/>.
- ²³R. H. Silsbee, *J. Appl. Phys.* **32**, 1459 (1961).
- ²⁴D. L. Griscom, in *Glass Science and Technology*, edited by D. L. Uhlmann and N. J. Kreidl (Academic, New York, 1990), Vol. 4B, p. 151.
- ²⁵H. Hosono, H. Kawazoe, K. Oyoshi, and S. Tanaka, *J. Non-Cryst. Solids* **179**, 39 (1994).
- ²⁶E. Holzenkampfer, F. W. Richter, J. Stuke, and U. Voget-Grote, *J. Non-Cryst. Solids* **32**, 327 (1979).
- ²⁷D. L. Griscom, E. J. Friebele, K. J. Long, and J. W. Fleming, *J. Appl. Phys.* **54**, 3743 (1983).
- ²⁸A. Stesmans and V. V. Afanas'ev, *Appl. Phys. Lett.* **69**, 2056 (1996).
- ²⁹M. Jivanescu, A. Stesmans, and M. Zacharias, *J. Appl. Phys.* **104**, 103518 (2008).
- ³⁰K. L. Brower, *Appl. Phys. Lett.* **43**, 1111 (1983).
- ³¹A. Stesmans, *Phys. Rev. B* **48**, 2418 (1993).
- ³²C. R. Helms and E. H. Poindexter, *Rep. Prog. Phys.* **57**, 791 (1994).
- ³³K. L. Brower, *Phys. Rev. B* **33**, 4471 (1986).
- ³⁴A. Stesmans, B. Nouwen, and V. V. Afanas'ev, *Phys. Rev. B* **58**, 15801 (1998).
- ³⁵E. H. Poindexter and P. J. Caplan, in *Insulating Films on Semiconductors*, edited by M. Schultz and G. Pensl (Springer, New York, 1981), p. 150.
- ³⁶A. Stesmans and V. V. Afanas'ev, *Phys. Rev. B* **57**, 10030 (1998).
- ³⁷A. Stesmans and V. V. Afanas'ev, *J. Appl. Phys.* **83**, 2449 (1998).
- ³⁸W. Futako, N. Mizuochi, and S. Yamasaki, *Phys. Rev. Lett.* **92**, 105505 (2004).
- ³⁹V. V. Afanas'ev, A. Stesmans, and M. O. Andersson, *Phys. Rev. B* **54**,

- 10820 (1996).
- ⁴⁰M. R. Mucalo, D. G. McGavin, and N. B. Milestone, *J. Mater. Sci.* **32**, 3271 (1997).
- ⁴¹R. Blinc, D. Arcon, P. Cevc, I. Pocsik, M. Koos, Z. Trontelj, and Z. Jaglicic, *J. Phys.: Condens. Matter* **10**, 6813 (1998).
- ⁴²D. L. Griscom, *J. Non-Cryst. Solids* **31**, 241 (1978).
- ⁴³D. L. Griscom, *Phys. Rev. B* **22**, 4192 (1980).
- ⁴⁴A. Stesmans and V. V. Afanas'ev, *J. Appl. Phys.* **97**, 033510 (2005).
- ⁴⁵D. L. Griscom, E. J. Friebele, and G. H. Sigel, *Solid State Commun.* **15**, 479 (1974).
- ⁴⁶D. L. Griscom, *Nucl. Instrum. Methods Phys. Res. B* **1**, 481 (1984).
- ⁴⁷A. Stesmans, K. Clemer, and V. V. Afanas'ev, *Phys. Rev. B* **77**, 094130 (2008).
- ⁴⁸A. Stesmans and F. Scheerlinck, *Phys. Rev. B* **50**, 5204 (1994).
- ⁴⁹M. E. Zvanut and T. L. Chen, *Generation and Annealing Kinetics of Oxygen Vacancy and Oxygen Excess Centers in Thin Film SiO₂* (Trans Tech, Zurich-Uetikon, 1997), p. 7; K. Clémer, A. Stesmans, V. V. Afanas'ev, L. F. Edge, and D. G. Schlom, *J. Appl. Phys.* **102**, 034516 (2007).
- ⁵⁰S. P. Karna, H. A. Kurtz, W. M. Shedd, R. D. Pugh, and B. K. Singaraju, *IEEE Trans. Nucl. Sci.* **46**, 1544 (1999).
- ⁵¹A. Stirling and A. Pasquarello, *Phys. Rev. B* **66**, 245201 (2002).
- ⁵²P. J. Caplan, E. H. Poindexter, B. E. Deal, and R. R. Razouk, *J. Appl. Phys.* **50**, 5847 (1979).
- ⁵³A. Stesmans, *Phys. Rev. B* **45**, 9501 (1992).
- ⁵⁴M. Mizuguchi, H. Hosono, and H. Kawazoe, *Mater. Sci. Eng., B* **54**, 38 (1998).
- ⁵⁵J. E. Wertz and J. R. Bolton, *Electron Spin Resonance. Elementary Theory and Practical Applications*, 2nd ed. (Chapman and Hall, London, 1986).
- ⁵⁶H. J. von Bardeleben, J. L. Cantin, J. J. Ganem, I. Trimaille, and E. P. Gusev, in *Defects in High-k Gate Dielectric Stacks*, edited by E. Gusev (Springer, Dordrecht, 2006), Vol. 220, p. 249.
- ⁵⁷H. Hosono and R. A. Weeks, *Phys. Rev. B* **40**, 10543 (1989).
- ⁵⁸S. P. Karna, H. A. Kurtz, A. C. Pineda, W. M. Shedd, and R. D. Pugh, in *Defects in SiO₂ and Related Dielectrics: Science and Technology*, edited by G. Pacchioni, L. Skuja, D. L. Griscom, (Kluwer, Dordrecht, 2000), p. 599.
- ⁵⁹C. Kittel, *Phys. Rev.* **73**, 155 (1948).
- ⁶⁰I. Svare and G. Seidel, *Phys. Rev.* **134**, A172 (1964).
- ⁶¹R. B. Flippen, *Phys. Rev. B* **44**, 7708 (1991).
- ⁶²J. L. Stanger, J. J. Andre, P. Turek, Y. Hosokoshi, M. Tamura, M. Kinoshita, P. Rey, J. Cirujeda, and J. Veciana, *Phys. Rev. B* **55**, 8398 (1997).
- ⁶³C. Kittel and E. Abrahams, *Phys. Rev.* **90**, 238 (1953).
- ⁶⁴S. J. Wyard, *Proc. Phys. Soc. London* **86**, 587 (1965).
- ⁶⁵B. Movaghar, L. Schweitzer, and H. Overhof, *Philos. Mag. B* **37**, 683 (1978).
- ⁶⁶E. J. Friebele, D. L. Griscom, M. Stapelbroek, and R. A. Weeks, *Phys. Rev. Lett.* **42**, 1346 (1979).
- ⁶⁷P. W. Anderson and P. P. Weiss, *Rev. Mod. Phys.* **25**, 269 (1953).
- ⁶⁸R. Kubo and K. Tomita, *J. Phys. Soc. Jpn.* **9**, 888 (1954).
- ⁶⁹P. M. Richards and M. B. Salamon, *Phys. Rev. B* **9**, 32 (1974).
- ⁷⁰M. Stutzmann and D. K. Biegelsen, *Phys. Rev. B* **40**, 9834 (1989).
- ⁷¹T. Umeda, S. Yamasaki, J. Isoya, and K. Tanaka, *Phys. Rev. B* **59**, 4849 (1999).